Draft version December 1, 2017
Preprint typeset using LaTeX style emulateapj v. 01/23/15

MAGNETO-HYDRODYNAMICAL EFFECTS ON NUCLEAR DEFLAGRATION FRONTS IN TYPE IA SUPERNOVAE

Boyan Hristov [1,2], David C. Collins [2], Peter Hoeflich [2], Charles A. Weatherford [1], and Tiara R. Diamond[3]

Draft version December 1, 2017

ABSTRACT

This article presents the study of the effects of magnetic fields on non-distributed nuclear burning fronts as a possible solution to a fundamental problem for the thermonuclear explosion of a Chandrasekhar mass ($M_{\rm Ch}$) white dwarf (WD), the currently favored scenario for the majority of Type Ia SNe (SNe Ia). All existing 3D hydrodynamical simulations predict strong global mixing of the burning products due to Rayleigh-Taylor (RT) instabilities, which is in contradiction with observations. As a first step and to study the flame physics we present a set of computational magneto-hydrodynamic (MHD) models in rectangular flux tubes, resembling a small inner region of a WD. We consider initial magnetic fields up to 10^{12} G of various orientation. We find an increasing suppression of RT instabilities starting at about 10^9 G. The front speed tends to decrease with increasing magnitude up to about 10^{11} G. For even higher fields new small scale finger-like structures develop, which increase the burning speed by a factor of 3 to 5 above the field-free RT-dominated regime. We suggest that the new instability may provide sufficiently accelerated energy production during the distributed burning regime to go over the Chapman-Jougey limit and trigger a detonation. Finally we discuss the possible origins of high magnetic fields during the final stage of the progenitor evolution or the explosion.

Subject headings: instabilities, magnetic fields, magneto-hydrodynamics, turbulence, white dwarfs

1. INTRODUCTION

Type Ia supernovae (SNe Ia) are spectacular explosions at the end of the life of stars. Similar explosion energies, spectra, light curves (LC) and LC decline rates, Δm_{15}, make them standard candles capable of measuring the Universe at the largest cosmological scales (Phillips 1993). Nevertheless there is no theory for the physics of SNe Ia to explain fully the observations. Recently Li et al. (2003, 2011), Foley et al. (2013) and Howell et al. (2006) identified the Iax and the super-Chandrasekhar mass ($M_{\rm Ch}$) subclasses which further complicates our understanding of these objects.

It is widely accepted that a Type Ia supernova is a thermonuclear explosion resulting from a binary system, of which one star is necessarily a degenerate carbon-oxygen (*C-O*) white dwarf (WD) (Hoyle & Fowler 1960). Current research considers various progenitor configurations and final outcomes. Depending on whether or not both stars are WDs, the progenitor system is called double degenerate (DD) or single degenerate (SD). In addition, proposed scenarios are distinguishable by the ignition mechanism and other characteristics. In the case of a DD progenitor system, a dynamical merger or a violent collision between the WDs is capable of releasing enough heat to trigger an ignition. This process can end up as a SN Ia, a highly magnetized WD (MWD), or an accretion-induced collapse (AIC) (Iben & Tutukov 1984; Webbink 1984; Benz et al. 1990; Rasio & Shapiro 1994; Segretain et al. 1997; Yoon et al. 2007; Wang et al. 2009b,a; Lorén-Aguilar et al. 2009; Isern et al. 2011; Pakmor et al. 2011). Another class of SNe Ia scenarios is the double detonation of a sub-$M_{\rm Ch}$ WD with accretion from a helium (He) companion. A detonation in the surface helium layer causes a secondary detonation in the core (Woosley et al. 1980; Nomoto 1982a; Livne 1990; Woosley & Weaver 1994; Hoeflich & Khokhlov 1996; Kromer et al. 2010; Woosley & Kasen 2011). Finally there is the $M_{\rm Ch}$ explosions scenario, where the WD progenitor accretes material from a companion star and nuclear surface burning to C/O leads to an increase of the WD mass. This can happen in either a SD system, where the donor star is a main-sequence star, a red giant, etc., or in a DD system with another WD being the donor (Whelan & Iben 1973; Piersanti et al. 2003). With increasing WD mass the electron gas in the central region becomes increasingly relativistic, which leads to faster compressional heat release, a raise of the central temperatures, and the triggering of a central C/O deflagration front when the mass of the progenitor approaches $M_{\rm Ch}$. (Hoyle & Fowler 1960; Sugimoto & Nomoto 1980; Nomoto 1982b; Hoeflich & Stein 2002; Piersanti et al. 2003). It is likely that the dynamical merger, $M_{\rm Ch}$ explosion, and double-detonation channels all contribute to the SN Ia population because of the "stellar amnesia"effect (Hoeflich (2006), and references therein).

In this paper, we will focus on the $M_{\rm Ch}$ explosion channel because of its consistency with a wide range of observations and their statistical properties. From observations we learn that the ejecta of a typical SNe Ia is made of chemical layers (e.g. Barbon et al. 1990; Kirshner et al. 1993; Hoeflich 1995; Fisher et al. 1997; Hoeflich et al. 2002; Marion et al. 2003; Stehle et al. 2005; Tanaka et al. 2011). The overall density structure shows small deviations from spherical geometry based on the continuum polarization (Howell et al. 2001; Maund et al. 2010; Patat et al. 2012) and based on close to spherical supernovae remnants (Rest et al. 2005; Badenes et al. 2006; Fesen et al. 2007; Rest et al. 2008).

[1] Department of Physics, Florida A&M University
[2] Department of Physics, Florida State University
[3] NASA Goddard Space Flight Center, Greenbelt, MD 20771, USA

Despite the success of $M_{\rm Ch}$ explosions, there are serious problems related to mixing by Rayleigh-Taylor (RT) instabilities during deflagration burning prior to the phase of strong expansion which results in a freezing out of the rising plumes and in strong large-scale mixing of the ejecta as in Khokhlov (1995); Niemeyer & Hillebrandt (1995); Livne (1999); Reinecke et al. (1999); Gamezo et al. (2003); Röpke et al. (2006); Plewa (2007). Although a layered chemical structure is partially restored during the detonation phase (Gamezo et al. 2005; Röpke et al. 2012), the predicted imprint of deflagration mixing is in contradiction to observations. Observations of local SNe Ia strongly suggest a process to partially suppress the dominant role of RT instabilities during the deflagration. These observations include: a) direct imaging of the SNR s-Andromeda, which shows a large 'Ca-free' core, indicative of high-density burning and limited mixing (Fesen et al. 2007, 2015); b) post-maximum spectra in normal-bright and subluminous SNe Ia. In particular, injection of radioactive material into the S/Si layer result in significantly degraded spectral fits to the observations (Figs. 12 and 14 Hoeflich et al. 2002); and c) flat-topped or stubby line profiles $1-2$ years after the explosion, which indicate stable isotopes remaining near the center after the initial phase of burning (Hoeflich et al. 2004; Motohara et al. 2006; Maeda et al. 2010, 2011; Penney & Hoeflich 2014; Stritzinger et al. 2014; Diamond et al. 2015). The good agreement has been obtained with spherical models, whereas the flame physics is inherently multi-dimensional which causes extensive mixing and strongly degrades individual fits and statistical properties. For a detailed discussion, see Höflich et al. (2006); Hoeflich et al. (2017).

Had there been a mechanism to suppress the RT instabilities in the early stages of the explosion, this discrepancy would be resolved. This requires a new piece of physics that has previously been left out by the current multi-dimensional models for the deflagration phase. High magnetic fields in nuclear burning fronts have been suggested for reactive fluids (Hoeflich et al. 2004; Remming & Khokhlov 2014; Hristov et al. 2016). Indeed, from both theory and simulation, magnetic fields have been shown to create effective surface tension, which suppresses RT instabilities parallel to the field and also secondary instabilities perpendicular to the field (Chandrasekhar 1961; Stone & Gardiner 2007a,b). We also note that magnetic surface fields in a wide range of strengths have been observed in WDs (Liebert et al. 2003; Kawka et al. 2007; Giammichele et al. 2012; Kepler et al. 2013; Sion et al. 2014; Ferrario et al. 2015; Kepler et al. 2016) but for most WDs they are small. Positron transport effects on light curves and spectral line profiles are expected at late times without magnetic fields (B) (see Milne et al. (1999); Penney & Hoeflich (2014)) but were not seen even in SN2011fe and SN2017j, which were observed for some three years past maximum light, respectively (Kerzendorf et al. 2017; Yang et al. 2017). Penney & Hoeflich (2014) used late-time near infrared line profiles to estimate magnetic fields. Though the number of SNe Ia with late-time IR spectra is small, recent observations strongly suggest that initial high magnetic fields with $B > 10^6$ G are common (Hoeflich et al. 2004; Penney & Hoeflich 2014; Diamond et al. 2015), even assuming fields on small-scales comparable to the pressure scale height of the WD.

Theories about the origin of WD magnetic fields and in support of amplification of the fields during different stages of the star or the binary system evolution are discussed in the final section.

The effects of magnetic fields on the nuclear burning in SNe Ia and in stellar context already exist. Potekhin & Chabrier (2012) investigate the effects of magnetic fields on non-resonant thermonuclear reactions in the interiors of *C-O* WDs. Kutsuna & Shigeyama (2012) study laminar flames in magnetic fields at densities that are typical for a $M_{\rm Ch}$ WD. Ji et al. (2013) simulated a MWDs merger on an axisymmetric cylindrical (2D) domain, followed by Zhu et al. (2015) in full 3D, who obtained final fields of $> 10^{10}$ G. Ghezzi et al. (2001, 2004) employ 1D semi-analytic flame models and find that the flame speed is affected by suppression of RT instabilities and additionally study the asymmetries of a deflagration front in a WD with a large-scale dipole field.

The article is organized in the following way. We describe our method in Section 2 starting with arguments about our choices of magnetic field strength and topology, the initial conditions and boundary conditions, and the regime of burning. The MHD solver and what we use out-of-the-box is outlined in Section 2.2 and the nuclear reaction model in Section 2.3. Our results are presented in Section 3. In Section 4, we discuss of the results, as well as future work and current dynamo theories. The latter is not part of this study but is important to justify the use of high magnetic fields in the central region of the WD. All equations are written in the *cgs* system of units. Other units are used in plots and throughout the text on occasion.

2. METHOD

To investigate the effects of magnetic fields on the nuclear burning we ran 16 models identical in all but the initial magnetic field magnitude and direction. These runs are listed in Table 1. One model has no magnetic field and the rest cover 5 magnitudes between 10^8 G to 10^{12} G; and vary between 3 directions: perpendicular to the WD radius, parallel to the WD radius and at 45°, labeled respectively $\widehat{\mathbf{y}}$, $\widehat{\mathbf{z}}$, and $\widehat{\mathbf{yz}}$. The main results can be sen in Figures 1 and 2. Figure 1 shows the burned fraction for projections along $\hat{y}$ (panel a) and $\hat{x}$ (panel b). Columns denote mean field orientatin, and rows denote field strength. Figure 2 shows the burning rate for each snapshot. These figures are at t=0.6 s. The bottom plot shows the position of the burning front in the computational domain. These will be discussed further in Section 3. To ensure the results are insensitive to the boundary, an additional simulation was executed based on model YZ10, but with twice the length of the domain. This longer domain did not change the results. Additionally we used a 1D model to measure the actual laminar front speed and thickness, which are approximately 10 km/s and 1 km, respectively.

2.1. *White dwarf setup*

Our work is in the context of a MWD undergoing a $M_{\rm Ch}$-scenario explosion. Model parameters were chosen to resemble the physical conditions of a WD after the onset of the deflagration stage, long enough for RT in-

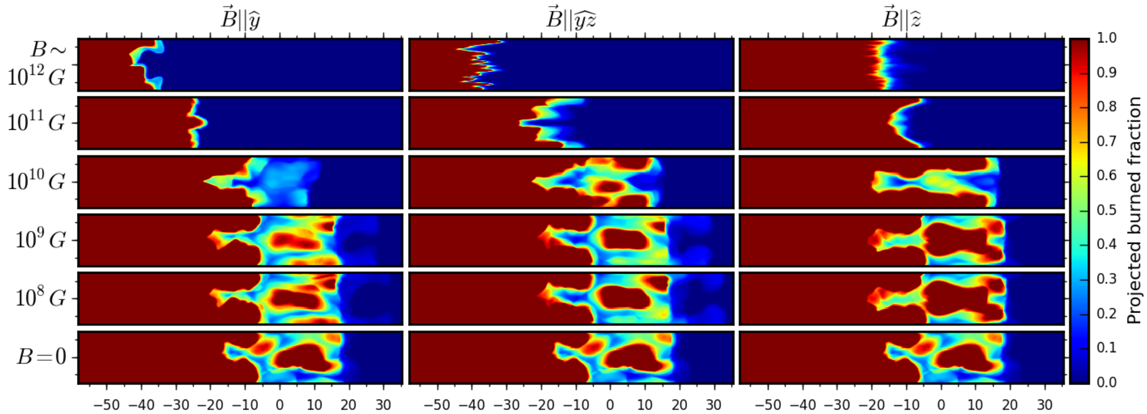

(a) Fuel molar fraction at $t = 0.6$ s projected along the y-axis.

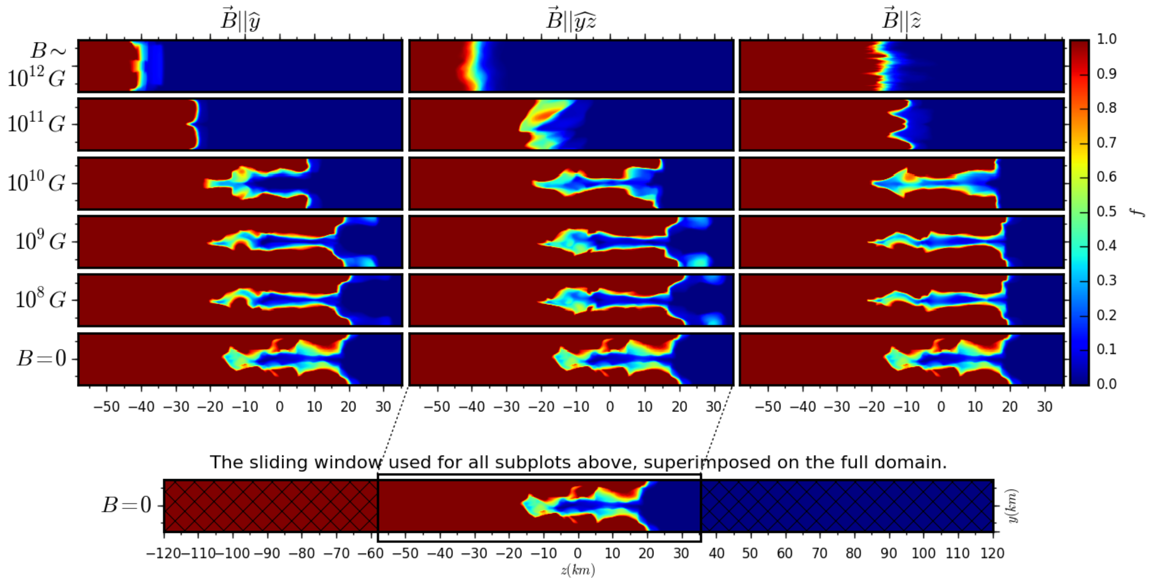

(b) Fuel molar fraction at $t = 0.6$ s projected along the x-axis.

FIG. 1.— Effects of B on the nuclear burning front. At low or no field (bottom row and up) one there is little difference in the behavior. Turbulence dominates and cusps of fuel appear. For models with 10^{10} G one can see some stabilization effects of the front, most notably in Y10. For models Y11 and Y12, where the field is in the plane of the front, the front becomes laminar. For models YZ12 and Z12, the strong-field models with a component of the field in the direction of the propoagation, we see another change in the burning properties. Smaller modes along z appear where the burning is accelerated. The modes are stabilized by the strong magnetic field. As a result, the fuel burns at an accelerated rate. We suggest that this may be a mechanism to accelerate the front over the Chapman-Jougey limit and trigger a transition to detonation. See also Fig. 2.

stabilities to set up and while the burning is still in the non-distributed regime.

As a first step we use a simplified picture in order to understand the physics of the burning front in the presence of a magnetic field – rectangular tubes with an initially uniform magnetic field, embedded in the inner region of a WD (Fig. 3.) We solve the models numerically using full 3D ideal MHD with non-distributed nuclear burning.

2.1.1. *Magnetic field magnitude*

We consider B magnitudes up to 10^{12} G, which is close to those for a virialized WD at $10^{13} - 10^{14}$ G (Alvear Terrero et al. 2015; Franzon & Schramm 2017). For a density of $\rho = 10^8$ g/cm^3, the equilibrium field is 2×10^{13} G.

MWDs are commonly observed in the magnitude range $10^3 - 10^9$ G (Liebert et al. 2003; Kawka et al. 2007; Giammichele et al. 2012; Kepler et al. 2013; Sion et al. 2014; Kepler et al. 2016), where the observations suggest a real cutoff at the upper bound and a sensitivity-limited lower bound (Ferrario et al. 2015). However, these observations are of non-exploding WDs, and the observed magnetic field magnitudes are only on the surface of the WD. Here, while we want to model a region close to the center and after a central ignition has occurred, which is a regime not probed by these observations. Small-scale dynamo theory, as well as virial analysis, suggest that fields as large as 10^{12}G are possible in the conditions expected before the explosion. This will be discussed further in Section 4.2.

2.1.2. *Field morphology considerations*

Field morphology can become very complex, as predicted by theory and observations (see Reinsch et al. 2005, and discussion therein). It is also uncertain whether the field is a dipole (or a multipole) on a large scale or turbulent, or if there is a combination of fields

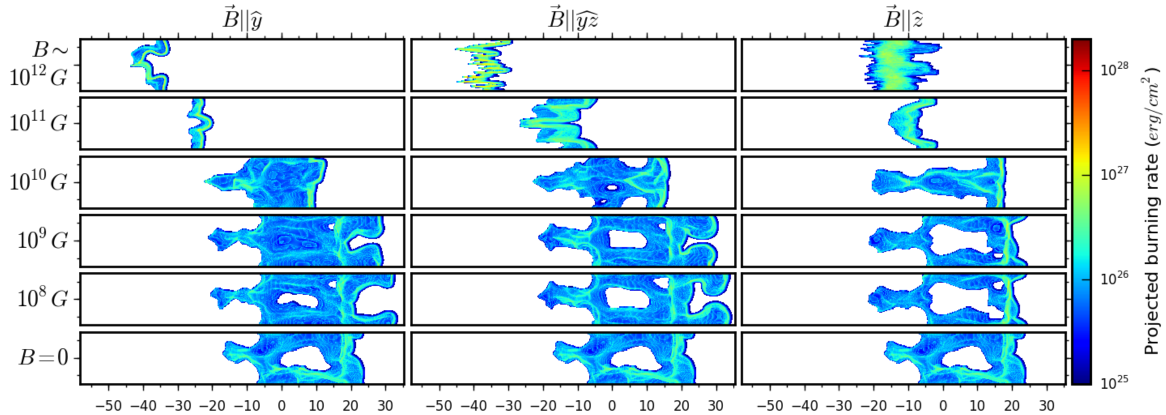

(a) Energy production density rate projected along the y-axis.

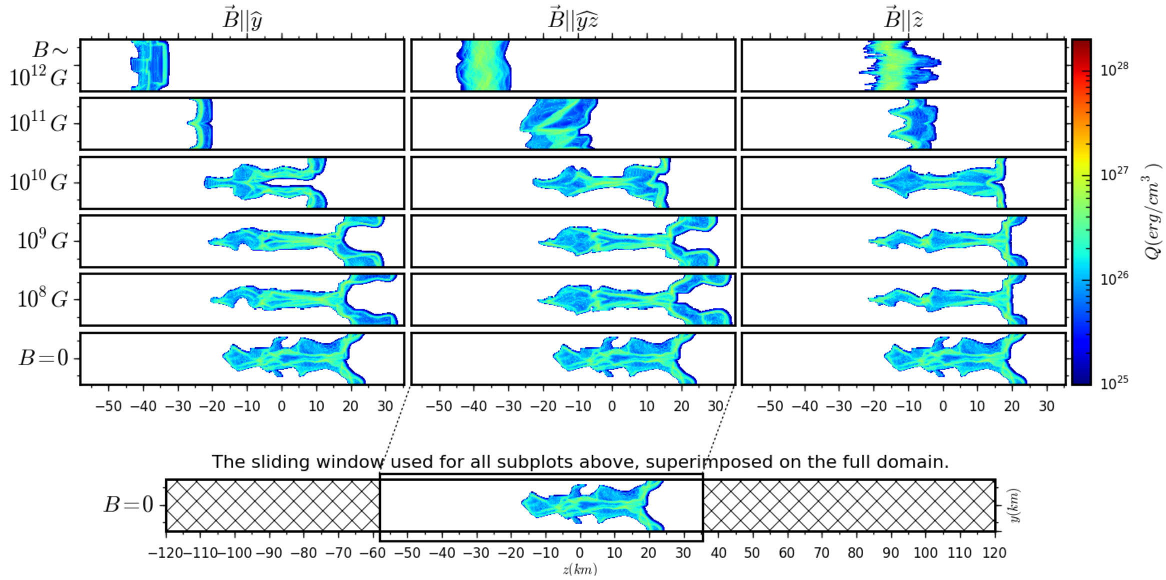

(b) Energy production density rate projected along the x-axis.

Fig. 2.— Energy production density rate projections at $t = 0.6$ s. See also Fig. 1.

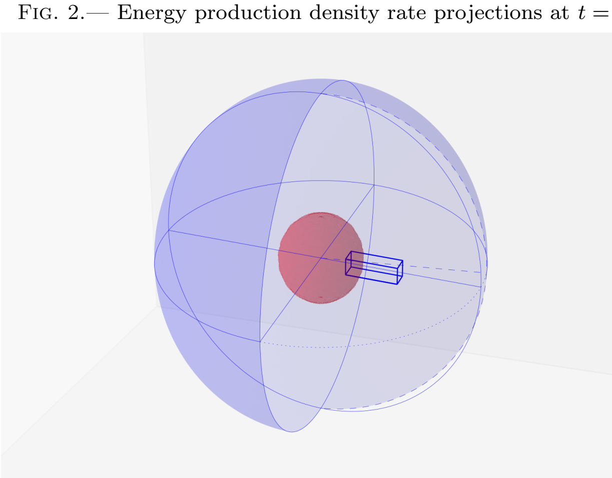

Fig. 3.— A sketch of the location of our flux tube within the white dwarf. This is close to the center, in the regime of non-distributed burning. See Section 2.1.3 for more details.

TABLE 1
Model (run) names, characterized by the size and orientation of the initial B-field.

Magnitude (Gauss)	Direction $\mathbf{B} \parallel \widehat{\mathbf{y}}$	$\mathbf{B} \parallel \widehat{\mathbf{yz}}$	$\mathbf{B} \parallel \widehat{\mathbf{z}}$
1.4×10^{12}	Y12	YZ12	Z12
1.4×10^{11}	Y11	YZ11	Z11
1.4×10^{10}	Y10	YZ10	Z10
3.5×10^{9}	Y9	YZ9	Z9
3.5×10^{8}	Y8	YZ8	Z8
0	$B = 0$	$(B = 0)$	$(B = 0)$

Note. — The front propagates in the $\widehat{\mathbf{z}}$ direction opposite to the gravitational acceleration, g. Figures 1 and 2 follow the same layout .

at different scales. We try to accommodate both cases by considering the order of the typical turbulent eddy, $l_{\rm turb} \sim 100$ km, established in Hoeflich & Stein (2002). Furthermore, the domain needs to be long enough to allow the advancement of the burning front for about a second, as well as to make the boundary effects remote enough. With this in mind we made our computational domain $240 \times 15 \times 15$ km.

2.1.3. *Initial and boundary conditions*

Immediately after a central ignition, RT instabilities would not develop because close to the center of the WD the gravitational acceleration, g $\simeq 0$. We need to pick a later time when the burning front becomes RT-unstable. In addition we are interested in the early evolution of the WD, because plumes created early on have the most time to rise and therefore would create the most mixing. Such conditions are realized in a model in Hoeflich (2006) at time $t = 0.1$ s when the burning front has reached about 1700 km from the center of the WD. At that time and location g and ρ change little within the span of the domain, L_z, so we initialize them with constants g $\approx 1.9 \times 10^9$ cm/s^2 and $\rho_0 \approx 10^8$ g/cm^3. Additionally we keep $\mathbf{g}$ constant in time.

We place the burning front at 10 km from the bottom and perturb its plane, so the initial front surface is described by $\zeta(x, y)|_{t=0} = A_0(\cos(k_0 x)) + \cos(k_0 y)$, where $k_0 = 2\pi/\lambda_0$. We initialize the region below the burning front with completely burned material and the one above with unburned fuel. Both regions have an initial density of $\rho_0 = 10^8$ g/cm^3.

2.1.4. *Non-distributed regime of burning*

At the burning front, with temperatures of $T \gtrsim 10^{9.5}$ K and densities of $\rho_0 \approx 10^8$ g/cm^3, the burning rate is so high that the laminar front thickness drops to the order of centimeters: $l_{\mathrm{flame}} \sim 10^{-3} - 10$ cm (Timmes & Woosley 1992). This is so much smaller than other length scales that an attempt to capture the details of the burning front would be a formidable computational task. As a consequence, and with the burning being complete in this regime, we cannot resolve any intermediate isotopes but only fuel and burning products. We need a grid resolution, Δx, small enough to reproduce accurate MHD features, but much coarser that the front scale length, $\Delta x \gg l_{\mathrm{flame}}$, and we use the one from Khokhlov (1995).

2.2. *Code*

For the data presented in this paper, we solve the ideal MHD equations with nuclear burning using the adaptive mesh refinement (AMR) code Enzo (Bryan et al. 2014) extended to MHD by Collins et al. (2010). The nuclear burning is a new addition to the code, and described in Section 2.3. The MHD solver uses the hyperbolic solver of Li et al. (2008), the isothermal HLLD Riemann solver developed by Mignone (2007), and the Constrained Transport (CT) method of Gardiner & Stone (2005). The simulations presented here were run with fixed resolution. Enzo has been used in a diverse array of astrophysical settings, including star formation (Abel et al. 2002; Collins et al. 2012), supersonic turbulence (Kritsuk et al. 2007), x-ray gas in clusters, (Bryan & Norman 1998), and large-scale structure (Bryan et al. 1999; O'Shea et al. 2015), and the epoch of reionization (Norman et al. 2015), among others.

The MHD equations with burning are as follows:

$$\frac{\partial \rho}{\partial t} + \nabla \cdot (\rho \mathbf{v}) = 0 \tag{1}$$

$$\frac{\partial \rho \mathbf{v}}{\partial t} + \nabla \cdot \left(\rho \mathbf{v}\mathbf{v} + \mathbf{I}P - \frac{\mathbf{B}\mathbf{B}}{8\pi} \right) = -\rho \mathbf{g} \tag{2}$$

$$\frac{\partial E}{\partial t} + \nabla \cdot \left[(E + P)\mathbf{v} - \frac{\mathbf{B}(\mathbf{B} \cdot \mathbf{v})}{4\pi} \right] = -\rho \mathbf{v} \cdot \mathbf{g} + \dot{Q} \tag{3}$$

$$\frac{\partial \mathbf{B}}{\partial t} + \nabla \times (\mathbf{v} \times \mathbf{B}) = 0 \tag{4}$$

where $\mathbf{vv}$ and $\mathbf{BB}$ are the velocity and the magnetic field outer products and ρ, $\mathbf{g}$, and $\dot{Q}$ are the density, the gravitational acceleration, and the energy production rate from the nuclear burning. The total energy density is equal to the total of the kinetic, the thermal and the magnetic energy,

$$E = e + \frac{\rho v^2}{2} + \frac{B^2}{8\pi} \tag{5}$$

and

$$P = p + \frac{B^2}{8\pi} \tag{6}$$

is the total pressure, which is the thermal plus the magnetic pressure.

A particular realization of a degenerate relativistic equation of state (EOS) from Hoeflich (2006) is shown in Fig. 4. Considering the right two panels, one can assume that at temperatures $T \gtrsim 10^{9.5}$ K and at densities in the range $\rho = 10^7 - 10^8$ g/cm^3, the adiabatic index $\gamma = \mathrm{const}$ is a reasonable approximation. Hence we close the system with the equations of state for an ideal gas,

$$e = \frac{p}{\gamma - 1} \tag{7}$$

2.3. *Burning*

We model the nuclear burning and flame propagation after Khokhlov (1995), which takes advantage of the non-distributed regime in a couple of ways. Firstly it takes a grid resolution much coarser than the flame scale length, as discussed in Section 2.1.4. Then it approximates the real nuclear network with one that has only two elements:

$$\text{fuel} \rightarrow \text{product} + \mathcal{Q} \tag{8}$$

where $\mathcal{Q}$ is the specific energy produced from burning. In our simulations the fuel consists of equal amounts by number of ^{12}C and ^{16}O with a mean atomic weight $\mathcal{A}_{\mathrm{fuel}} \approx 14$, and the product is ^{56}Ni. Let's define the burned molar fraction, simply referred as burned fraction, f, as

$$f = \frac{\mathcal{Y}_{\mathrm{prod}}}{\mathcal{Y}_{\mathrm{fuel}} + \mathcal{Y}_{\mathrm{prod}}} \tag{9}$$

where $\mathcal{Y}_i$ are the abundances. Note that $f \in [0, 1]$, where $f = 0$ corresponds to pure fuel, and $f = 1$ means pure product. A nuclear deflagrating flame ignites unburned fuel by heating through electron conduction. The model flame spreads by diffusing the burned fraction, f:

$$\frac{\partial f}{\partial t} + \mathbf{v} \cdot \nabla f = K \nabla^2 f + R. \tag{10}$$

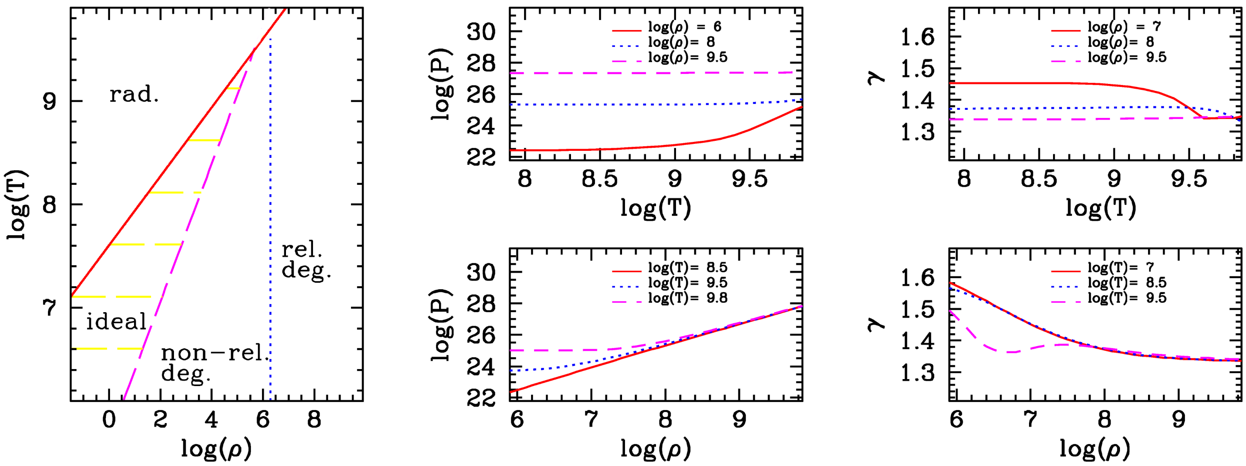

FIG. 4.— EOS of a WD (Hoeflich 2006). The two right panels show that γ depends relatively weakly on T and on ρ in the non-distributed regime of burning ($T \geq 10^{8.5}$ K and $\rho \sim 10^8$ g/cm^3), hence it can be taken to be a constant.

Here K approximates the diffusion of burning material, thus energy to ignite the up-stream fuel. The instantaneous burning rate is then denoted by R. The front becomes stretched over a few grid cells, as is typical for shock-capturing schemes. The laminar speed velocity should be proportional to $\sqrt{KR}$. We chose a value of 10 km/s, which we confirmed in a 1D run. According to Remming & Khokhlov (2016), the laminar front velocity depends on the magnetic field strength and direction in addition to the fuel density. However in our regime the difference the authors had calculated is about 3%, allowing us to assume constant values for K and R. Additionally we turn R on and off locally depending on the burned fraction:

$$R = R(f) = \begin{cases} R_0, & \text{if } f_0 \leq f \leq 1; \\ 0, & \text{if } 0 \leq f < f_0 \end{cases} \quad (11)$$

This delays the ignition of the fuel locally, preventing the entire domain from been ignited in the first few time steps by non-physical numerical waves traveling faster than the physical laminar flame. Finally, the burning energy is calculated as:

$$\dot{Q} = \mathcal{Q}\frac{d\rho_{\rm prod}}{dt} \quad (12)$$

3. RESULTS

As described in Section 2, Figures 1 and 2 show the effect of magnetic field on the propagation of nuclear burning in our simulations. There is a clear impact of the magnetic field on the speed and morphology of the front in the strongest field simulations, but one can see that all of the tested fields leave some imprint on the burning front regardless of the initial magnitude or direction. At low magnetic field, ($B \lesssim 10^9$ G, and including no field at all, bottom row in those figures), the inverted initial pressure gradient across the front makes the flow RT-unstable. Large modes grow faster, as expected, and they would continue to rise. The flame morphology becomes increasingly complex. The burning front develops chaotic structure and is dominated by turbulence. Small modes grow slower and are washed out by the flow shear or the diffusion by which the laminar front advances (Khokhlov 1995, see also eqn. 11) The effective front width is $\sim 50-70$ km. Some pockets of fuel are formed.

Going up in magnitude to 10^{10} G, we can recognize a trend of the effective width of the burning front shrinking. This is most pronounced in the case of a transverse field. Turbulence is still prominent, and the front is comparable to that of the lower B cases.

At the highest magnetic field strengths, stabilization effects are well manifested. The chaotic behavior is suppressed, and the front structure is closer to laminar. The effective front width is now only on the order of 10 km. For models Y11, YZ11 and Y12 the flame front closely follows the field lines.

For models Z12 and YZ12 we identify another change in the behavior. The front becomes jagged with smaller peaks oriented along z. In YZ12 these are seen only in the y-projection. This behavior is mirrored in the front velocity and energy production, shown in Figures 5 and 6, respectively. In Figure 5, the black line shows the velocity of the fiducial un-magnetized run. After an initial transient phase, as the instability sets in prior to t=0.3 s, it is clearly seen that the moderately magnetized runs (blue lines at 10^{10} G and purple lines at 10^{11}G) move slower due to the decreased surface area of the front. This decrease is also seen in the energy production rate, which can be seen as a proxy for the surface area, see eqn. 11. In these runs, the instability is suppressed as expected by perturbation analysis, discussed in Section 3.1. For the largest field runs that also contain a component along the propagation direction, however, the behavior is somewhat counterintuitive. These runs show a significant *increase* in the front velocity over all other runs. This is due to suppression of secondary Kelvin-Helmholtz instability, see Section 3.2.

3.1. *Linear Stability Analysis*

The MHD equations (1-4) can be perturbed about an interface subject to an acceleration, and the growth rates calculated, as is done in standard Rayleigh-Taylor or Kelvin-Helmholtz instability studies. The magnetic field can exert tension in the front, and tend to stabilize the flow. Details are left to Appendix C, but we will discuss the salient results here. The analysis assumes that

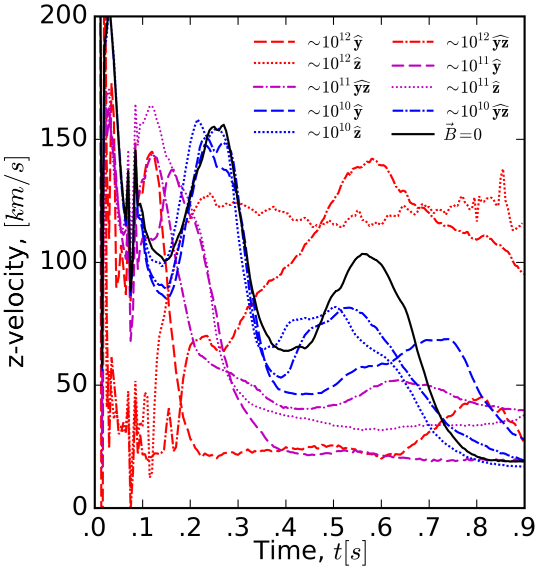

FIG. 5.— Flame speed in the frame comoving with the bulk flow. The 10^8 G and 10^9 G profiles are omitted for clarity. For most simulations, the velocity is decreased over the non-magnetized case by the reduction of the surface area of the front. The Z12 and YZ12 velocities are larger than any other case as these regimes have new kind of instability as discussed in Section 3.1.

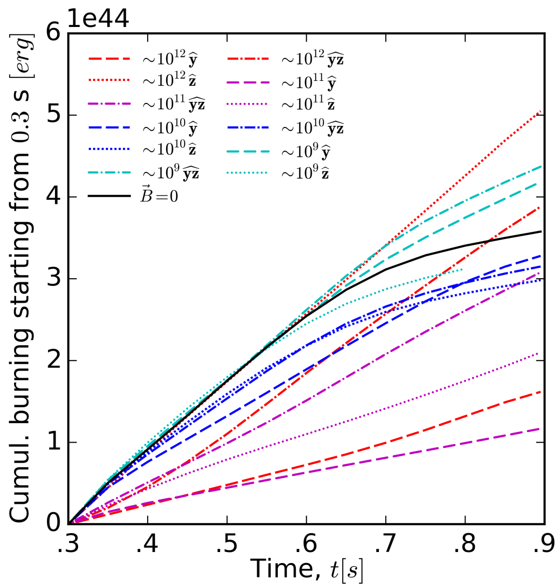

FIG. 6.— Cumulative burning energy, integrated from $t = 0.3$ s. The 10^8 G profile is not shown for clarity. In order to remove the effects of the initial conditions, seen in Fig. 5, we integrate the burning rates starting right after the burst. We note a trend for the rates to drop with increasing field magnitude up to 10^{11} G. Beyond that models Z12 and YZ12 show the steepest slopes as well as steady state processes.

the magnetic field is either parallel or perpendicular to the gravity, g and the position of the front is assumed to behave as $exp(ik_x x + ik_y y + \Omega t)$. Here, a negative Ω indicates a stable mode. The dispersion relation for the field perpendicular to **g**, shown in the bottom panel of Fig. 7, shows that the only simulations with some stable modes in the linear regime are Y11, YZ11 and Y12. All other orientations, at all modes, remain unstable. This explains the stark contrast between the top two rows and the other four in Figures 1 and 2.

To explain the increased burning seen in runs Z12 and YZ12, we look at the dispersion relation for fields parallel to **g** in the top panel of Fig. 7. No matter the field strength and orientation, the flow is always unstable. The smallest modes grow the fastest, which is opposite to when the field is perpendicular to the gravity. At the same time, the smaller the mode the easier it is destroyed via lateral forces as well as flame diffusion.

3.2. *Nonlinear Growth*

The linear stability is useful for guiding intuition, but the flow in question is no longer in the linear regime.

In order to quantify this impression we applied a Fourier transform to the 95% iso-surface of the burned fraction in all 10^{11} and 10^{12} runs, shown in Fig. 8. This is a good method for the YZ12 and Z12 models, since the said iso-surface is a single-valued function, $\zeta(x, y)$. When the front has multiple points for the same (x, y) we take the rightmost one. Most profiles have the same power for the medium modes in the range $L/\lambda = 8 - 15$ zones. However these are dominated by the larger modes ($L/\lambda = 1 - 6$ zones) and appear as noise. The Z12 spectrum, on the other hand, shows suppressed large modes to the same level power as the medium modes. Therefore we cannot consider the latter as noise.

Furthermore the side walls of these instabilties become almost parallel to $\widehat{\mathbf{z}}$, where the sinking fuel and the rising burned material create shear at the boundary. These conditions are right for developing Kelvin-Helmholtz instabilities, but the magnetic field is now almost parallel to the shear interface, adding surface tension and making the flow laterally stable. The condition for Kelvin-Helmholtz stability, derived in the stability analysis in the Appendix (in Eq. C5) is visualized in a 1-zone slice in Fig. 9. It holds for all zone boundaries parallel to $\widehat{\mathbf{z}}$. Somewhat similar effects to the RT fingers were observed by Stone & Gardiner (2007a,c), however in the lateral direction and in different regimes.

We also observe that all spectra become flat for $L/\lambda > 15$ with the least power in those modes. Since the lateral advection is suppressed we could attribute this effect to diffusion, however it could be something else, including numerical.

Fig. 9 shows fingers of fuel narrower than the flame laminar thickness, 3–4 zones. Poludnenko & Oran (2011) and Hicks (2015) found that when the radius of curvature at the bottom of the fingers becomes on the order of the laminar flame thickness or less, the fuel burns at an accelerated rate. The plots in Figures 5 and 6 confirm this. We note that the the burning rates and the front speeds tend to drop with magnitude and are smallest at about 10^{11} G due to the decrease of the front surface, but in the Z12 and YZ12 models the profiles become steeper again.

4. DISCUSSION

We show that a magnetic field in the WD deflagration regime has an effect on nuclear burning for magnitudes $B \gtrsim 10^{10}$ G. At medium to high magnitudes we observe a front that is more organized compared to low magnetic field strength or no field at all. The burning

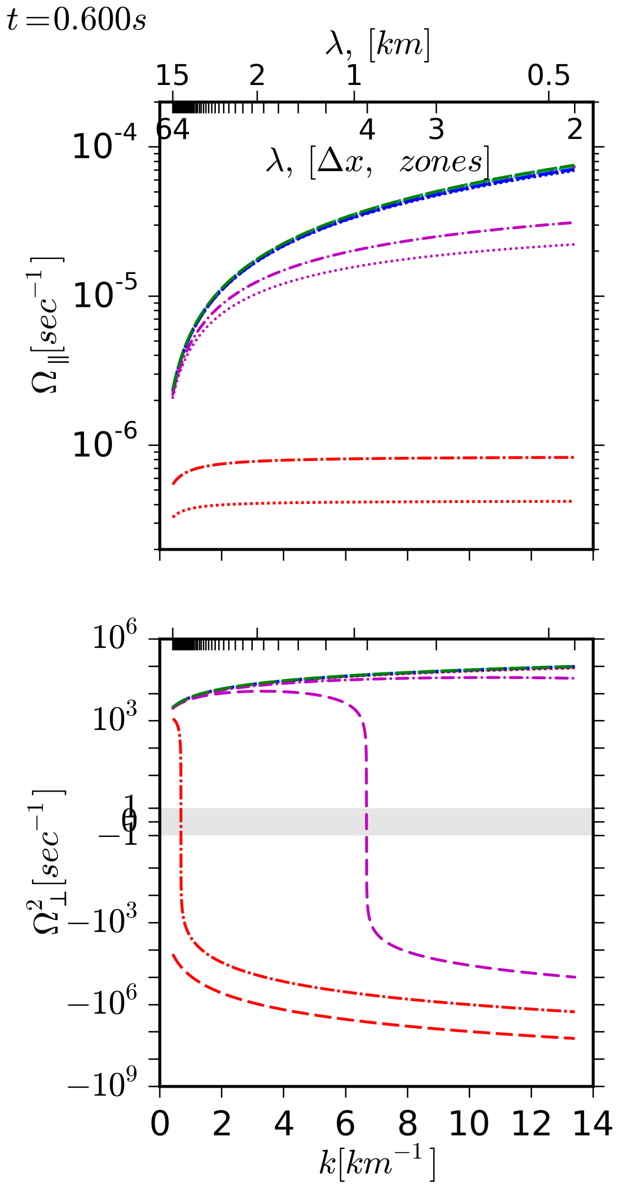

FIG. 7.— Growth rate of perturbation modes. See legend on Fig. 6. Negative values indicate stable modes. The theoretical dispersion relations are used for magnetic fields parallel (Eqs. C1–C3), and perpendicular (Eq. C4) to $\mathbf{g}$ at $t = 0.6$ s. The wavelength range starts from 2 computational cells up to the entire domain width. For the perpendicular cases (bottom panel) we see that stable modes can be expected only in three simulations, whereas all modes are stable in the Y12 run. This is a rough agreement with the flows shown in Fig. 1, especially in the $\widehat{\mathbf{y}}$ models. We also see stable surfaces along the magnetic field in the YZ11 run. In the parallel cases (top panel) none of the simulations show stable modes, however the growth rate is suppressed by at least an order of magnitude in the Z12 and YZ12 runs. The smallest modes grow the fastest. To subsequent stabilization of the vertical fingers (see Fig. 9) leads to a new instability.

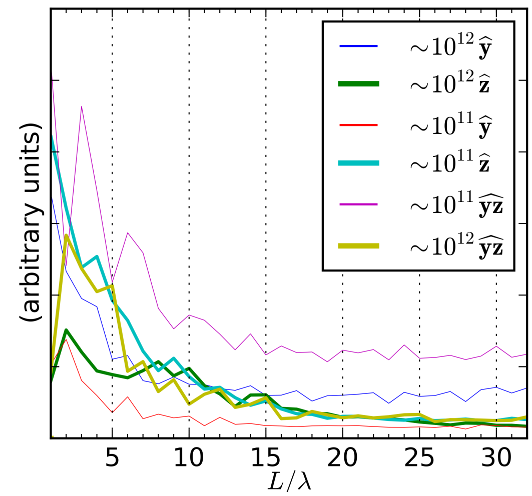

FIG. 8.— Fourier transformation of the flame as a function of x and y for the high-field simulations. All profiles are normalized so they have maximum 1, in order to emphasize the distribution of power within each simulation, rather than comparing powers between simulations. The Z12 spectrum shows stronger features for $L/\lambda = 8 - 15$ compared to the rest. This is due to the smallest modes having the highest growth rate in the linear theory and subsequent lateral magnetic support against secondary instabilities. Additionally all profiles become flat for $L/\lambda \geq 16$ with little power in that region, i.e. only modes larger than two computational cells are prominent. This can be attributed to competition of advection vs. diffusion, but could be a resolution effect as well.

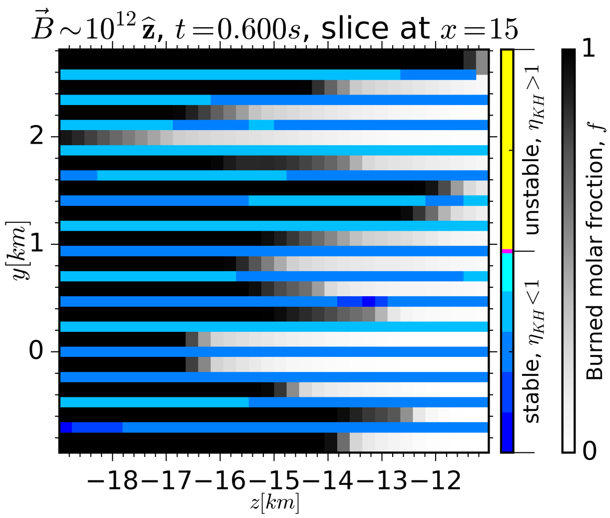

FIG. 9.— The "Kelvin-Helmholtz number" (Eq. C5, yellow-to-blue scale) on the computational cells boundaries superimposed on the burned fraction (gray scale) for the Z12 model at $t = 0.6$ s. Cold fuel sinks against the rising burned material, creating shear on the vertical cell boundaries. All lateral perturbations, i.e. the secondary Kelvin-Helmholtz instabilities, are suppressed by the magnetic field, sustaining the finger formations.

front becomes more laminar and less turbulent, and RT instabilities decrease. The effective front thickness also decreases by a factor of a few. One should ask whether medium fields are sufficient to bring significant change in the final outcome of the explosion, given that a Type Ia deflagration is estimated to only last about 2 seconds. The front speed and total burning rate tend to decrease as the field magnitude grows up to 10^{11} G regardless of the field direction. At 10^{12} G this trend is broken and the effects are also direction-dependent to a higher degree compared to the lower field strengths. When the longitudinal component of the field is strong, the burning is amplified and the front speed is highest and larger than the pure hydrodynamical case by a factor of 3 to 4.

4.1. *Impact of Magnetic Fields*

These results suggest that strong magnetic fields might be missing from the picture of WD explosion physics painted by current 3D models. Suppression of large modes of RT instabilities in the early stages of the explosion is necessary to prevent large scale mixing until the transition to detonation. If burning rate is amplified by magnetic fields it can lead to faster expansion and may freeze out the RT plumes in the unburned environment, consequently not allowing them rise to the surface, which also means less mixing.

A second possible implication is related to the development of small scale structures which result in an effective increase in the 'surface' of the flame, which is the physical underpinning for a significant increase of the burning rate compared to a pure hydrodynamical front.

Based on 3D full-star simulations of deflagration fronts, e.g. (Gamezo et al. 2003), pure deflagration fronts reach about 10–15 % effective burning speed if full scale RT instabilities have developed over $\approx 2-3$ seconds. As discussed in the introduction, the delayed-detonation model is currently the favorite for $M_{\rm Ch}$ explosions. Faster burning would increase the compression and trigger a detonation, the so called Chapman-Jougey limit. No solution for steady burning by deflagration exists above this limit, which for C/O rich mixtures is about 40 % of v_s (Bruenn 1972). Possible processes are still under discussion but are based on the Zel'dovich mechanism, i.e. mixing of burned and unburned matter on small scales to increase the effective nuclear burning rate. Possible physical causes for mixing include mixing during a pulsational phase of the WD, crossing shock waves produced in the highly turbulent medium, or shear flows and instabilities in the regime of distributed burning which are discussed in Poludnenko (2016). One requirement for the formation of a detonation front is simultaneous mixing over a significant volume. Small scale fluctuations may be expected to prevent a DDT through mixing (Khokhlov et al. 1997; Niemeyer & Woosley 1997). Our results of small scale structure with an effective increase of effective burning by factors of 3–5 in the case of high B fields may open an alternative mechanism for the DDT as a similar factor in the regime of distributed burning would bring the burning speed well above the Chapman-Jougey limit. Because the structure depends on the size and orientation of B, we must expect a wide variety and a dependence of the field morphology. A final answer is beyond this paper and will be addressed in full-star simulations in future works.

4.2. *Magnetic Field Growth and Saturation*

We have shown that B fields larger than $10^{9\ldots10}$ G will have a significant effect on the nuclear burning fronts under WD conditions, and may solve many of current problems with $M_{\rm Ch}$ explosions and delayed-detonation models in particular. As discussed in the introduction, some WD have magnetic fields but, for most WDs, the B fields are than those indicated by late-time observations of SNe Ia. Is it possible to produce high fields on relevant timescales prior to the explosion? Possible creation times for dynamos may be either during the accretion phase on time scales of 10^6 years, during the smoldering phase leading to the thermonuclear runaway on time scales of minutes (Hoeflich & Stein 2002), or during the hydrodynamical phase of instabilities during the explosion on time scales of seconds or less. This leads us directly to B-field amplification in WDs and dynamo theories.

A seed magnetic field can be amplified by a dynamo operating in the convective zone of a differentially rotating star, including WDs (Parker 1979; Thomas et al. 1995; Brandenburg & Subramanian 2005). In large scale dynamos, a toroidal field is produced by winding-up the poloidal component. The convective elements move upwards and downwards, perpendicular to the toroidal field lines, bending them and creating a new poloidal component (Parker 1979). Large scale dynamos grow with a typical timescale of the Alfvén times, $t_A \approx R(4\pi\rho)^{1/2}/B \approx 300$ s (Parker 1979), which is long compared to the smouldering phase.

Alternatively in so called small dynamos, turbulence alone can produce a small scale, unstructured magnetic field (Kazantsev 1968; Tayler 1973; Acheson 1978; Hawley et al. 1996; Spruit 2002; Brandenburg & Subramanian 2005; Braithwaite 2009; Beresnyak et al. 2009; Duez et al. 2010b,a). Within the core of a white dwarf close to $M_{\rm Ch}$, turbulence will undoubtedly play an enormous role. With viscosity $\nu = 3.13 \times 10^{-2}{\rm cm}^2{\rm s}^{-1}$ (Nandkumar & Pethick 1984; Isern et al. 2017), length scale L = 500 km and velocities V = 500 kms^{-1}, we find high Reynolds numbers of about $Re \equiv Lv/\nu = 10^{17}$. As the WD approaches M_{Ch}, $\gamma \to 4/3$, the stability against radial motions disappears. Then kinetic energy will undoubtedly exhibit a Kolmogorov cascade, $E = Ck^{-5/3}$, with energy distributed at all scales, k, in a power law down to the molecular dissipation scale. In recent theoretical studies, (e.g. Schekochihin & Cowley 2007; Beresnyak et al. 2009; Schober et al. 2012), it has been shown that the field can grow to energy equipartition in an eddy turnover time at the smallest scale, essentially instantaneously. Schober et al. (2012) estimate this growth rate, $\Gamma = \alpha {\rm Re}^{1/2}{\rm V/L}$. For values they cite for this rate, we find an exponential growth rate of $10^4{\rm s}^{-1}$. During the *kinematic dynamo* the Lorentz force is not large enough to affect the flow and can be treated as a passively amplified scalar, and analytic calculations can be performed. Once the field is in equipartition, no direct analytic solution exists, and phenomenological and numerical treatments must be performed. Schober et al. (2015) examine the feedback mechanism of Subramanian (1999), and find that in the small magnetic diffusivity limit as much as 40% of the total kinetic energy can be converted to magnetic energy. With $\rho = 10^9{\rm gcm}^{-3}$, this gives a magnetic field of 10^{12}G over a significant fraction of the core of the WD. Details of this saturation will be carried out in future simulations.

4.3. *Future Work*

We want to emphasize that this study presents only a first step to address the MHD problem for reactive fluids. Firm conclusions for an exploding WD require many more questions to be addressed. Here we will mention the limits of this study and questions which will be addressed in the near future by full-star models with our existing, more detailed nuclear networks. First, we treat the problem as if the WD was not expanding during the simulation – our gravitational acceleration is a constant instead of decreasing with time. Radial gradients in the gravitational acceleration, the initial density, and the initial pressure were neglected. Furthermore an evolved magnetic field would not be uniform, so the flame will encounter varying magnitude and direction as it advances. Moreover, the laminar diffusion speed will become directionally dependent. These effects will be studied in flux tubes using our Monte-Carlo transport coupled within a Particle in a Cell scheme. Finally, our nuclear network is too simple to carry out simulations in a distributed regime of burning should one want to include the detonation phase as well.

High resolution simulations of a full star are required in order to overcome the limitations of the flux tube results presented in this work. Other scientific questions we want to address in the future are: Are magnetic fields the missing physics in the current 3D models? In particular, do magnetic fields make pre-expansion of the WD possible; and if so, what is the mechanism – is it by suppressing the RT instabilities, by plume freeze-out on an accelerated background, or in some other way? What are observational signatures of the different field magnitudes and morphologies? Can they lead to different outcomes of the explosions, i.e. can different magnetic fields explain some of the diversity of SNe Ia?

ACKNOWLEDGEMENTS

C.A. Weatherford and B. Hristov were partially supported by the Department of Energy, National Nuclear Security Administration, under award DENA0002630, and the Nuclear Regulatory Commission, NRC-HQ-12-G-27-0091. P. Hoeflich acknowledges support by the National Science Foundation (NSF) grant 1715133. This work used the Extreme Science and Engineering Discovery Environment (XSEDE), which is supported by the NSF grant ACI-1548562. Simulations were performed on Stampede and Maverick at the Texas Advanced Computing Center (`https://www.tacc.utexas.edu`), using XSEDE allocation TG-AST140008. Thank you to Braithwaite for helpful discussions on the dynamo theories and the formation of ultra-high magnetic fields in WD, to S. Shore for helpful discussions on MHD instabilities, and Casey Mc Laughin for help with technical problems. Visualization was done using `yt` (Turk et al. 2011), `matplotlib` (Hunter 2007), and `numpy` (Van Der Walt et al. 2011). Thanks to Nathan Goldbaum and Matthew Turk for help on `yt` issues.

APPENDIX

MASS AND MOLAR FRACTION DEFINITIONS AND IDENTITIES

Here we define some quantities used in the text and give some conversions between them. Let's consider the fuel and product mixture, which we'll label with 1 and 2, respectively, to ease the notation. Obviously the partial mass densities add up to the total mass density:

$$\rho = \rho_1 + \rho_2 \tag{A1}$$

Then let's define the mass, the molar, and the burned fractions, $\mathcal{X}$, $\mathcal{Y}$, and f:

$$\mathcal{X}_i \equiv \rho_i/\rho, \quad \mathcal{Y}_i \equiv \mathcal{X}_i/\mathcal{A}_i \tag{A2}$$

$$f \equiv \frac{\mathcal{Y}_2}{\mathcal{Y}_1 + \mathcal{Y}_2} \tag{A3}$$

Clearly, the burned and the fuel fractions comprise the entirety of material, i.e. the fuel fraction equals to $1-f$, should one need it.

Using the definitions above it is easy to derive the following identities. The first two express the burned fraction, f, in terms of the total mass density, ρ, and one of the partial mass densities, ρ_1 or ρ_2. The following two equations show how to calculate the abundances, $\mathcal{Y}_{1,2}$, from the burned fraction, f.

$$f = \frac{\mathcal{A}_1(\rho-\rho_1)}{\mathcal{A}_1\rho - (\mathcal{A}_1-\mathcal{A}_2)\rho_1} = \frac{\mathcal{A}_1\rho_2}{\mathcal{A}_2\rho + (\mathcal{A}_1-\mathcal{A}_2)\rho_2} \tag{A4}$$

$$\mathcal{Y}_1 = \frac{1-f}{\mathcal{A}_1(1-f)+\mathcal{A}_2 f}, \mathcal{Y}_2 = \frac{f}{\mathcal{A}_1(1-f)+\mathcal{A}_2 f} \tag{A5}$$

BURNING OPERATOR

Provided that we know ρ, from Equations A1 and A4, it follows that we only need the mass fraction and one of the partial mass densities to determine the other one. In our implementation of the new burning operator in Enzo it is the product mass density, ρ_2, that is being stored and advected. The burning operator comes last in the time cycle and comprises the following steps: (i) find the burned fraction at the beginning of the cycle, using the second of Eq. A4; (ii) evolve the burned fraction using a 27-point stencil for the Laplacian; (iii) update the density from Eq. A5; and (iv) update the energy from Eq. 12.

LINEAR STABILITY THEORY

We use analytic linear stability results from Chandrasekhar (1961). These come from linear stability analyses of the growth rate, Ω, of normal perturbation modes, $\mathbf{k} \equiv k_x\widehat{\mathbf{i}} + k_y\widehat{\mathbf{j}}$ along the discontinuity interface, so that a perturbation is proportional to $\exp(ik_x x + ik_y y + \Omega t)$. Modes with such dependance on time are stable when $\Omega < 0$.

We split the magnetic field into two terms , parallel and perpendicular to the gravity, i.e. $\mathbf{B} \equiv B_z\widehat{\mathbf{k}} + \mathbf{B}_\perp$, where $B_z \neq 0$ and $\mathbf{B}_\perp \equiv B_x\widehat{\mathbf{i}} + B_y\widehat{\mathbf{j}} \neq \mathbf{0}$, respectively. The dimensionless dispersion relation for B_z is:

$$\begin{aligned}\eta^3 + 2\kappa(\alpha_2^{1/2}+\alpha_1^{1/2})\eta^2 + \kappa(2\kappa+\alpha_1-\alpha_2)\eta- \\ -2\kappa^2(\alpha_2^{1/2}-\alpha_1^{1/2}) = 0\end{aligned} \tag{C1}$$

where

$$\eta \equiv \frac{\Omega_\parallel}{\mathrm{g}/V_{A,z}}, \ \kappa \equiv \frac{k_\parallel}{\mathrm{g}/V_{A,z}^2}, \tag{C2}$$

$$V_{A,z}^2 \equiv \frac{B_z^2}{4\pi(\rho_2+\rho_1)}, \ \alpha_{1,2} \equiv \frac{\rho_{1,2}}{\rho_1+\rho_2}, \tag{C3}$$

and $\rho_1 < \rho_2$. In this case no values of the parameters B and $\rho_{1,2}$ yield stable modes.

We rewrite the dispersion relation for $\mathbf{B}_\perp$, for the modes parallel to the magnetic field, $\mathbf{k}_\perp \parallel \mathbf{B}_\perp$. Modes not parallel to $\mathbf{B}_\perp$ are "less" stable since the negative term should be multiplied by $\cos^2(\mathbf{B}_\perp, \mathbf{k}_\perp)$.

$$\Omega_\perp^2 = \mathrm{g}k_\perp \left(\frac{\rho_2 - \rho_1}{\rho_2 + \rho_1} - \frac{B_\perp^2}{2\pi(\rho_2 + \rho_1)g} k_\perp \right) \tag{C4}$$

Modes are stable when the right hand side of Eq. C4 is negative.

Finally we rewrite the condition for a mode to be Kelvin-Helmholtz stable as

$$\eta_{KH} \equiv \frac{\alpha_1 \alpha_2 \Delta v_z}{2V_A, z^2} < 1. \tag{C5}$$

REFERENCES

Abel, T., Bryan, G. L., & Norman, M. L. 2002, Science, 295, 93
Acheson, D. J. 1978, Royal Society of London Philosophical Transactions Series A, 289, 459
Alvear Terrero, D., Castillo García, M., Manreza Paret, D., Horvath, J. E., & Pérez Martínez, A. 2015, Astronomische Nachrichten, 336, 851
Badenes, C., Borkowski, K., Hughes, J., Hwang, U., & Bravo, E. 2006, ApJ, in press, astro-ph/0511140
Barbon, R., Benetti, S., Rosino, L., Cappellaro, E., & Turatto, M. 1990, A&A, 237, 79
Benz, W., Cameron, A. G. W., Press, W. H., & Bowers, R. L. 1990, ApJ, 348, 647
Beresnyak, A., Jones, T. W., & Lazarian, A. 2009, ApJ, 707, 1541
Braithwaite, J. 2009, MNRAS, 397, 763
Brandenburg, A., & Subramanian, K. 2005, Phys. Rep., 417, 1
Bruenn, S. W. 1972, ApJ, 177, 459
Bryan, G. L., Machacek, M., Anninos, P., & Norman, M. L. 1999, ApJ, 517, 13
Bryan, G. L., & Norman, M. L. 1998, ApJ, 495, 80
Bryan, G. L., Norman, M. L., O'Shea, B. W., et al. 2014, ApJS, 211, 19
Chandrasekhar, S. 1961, Hydrodynamic and hydromagnetic stability
Collins, D. C., Kritsuk, A. G., Padoan, P., et al. 2012, ApJ, 750, 13
Collins, D. C., Xu, H., Norman, M. L., Li, H., & Li, S. 2010, ApJS, 186, 308
Diamond, T. R., Hoeflich, P., & Gerardy, C. L. 2015, ApJ, 806, 107
Duez, M. D., Foucart, F., Kidder, L. E., Ott, C. D., & Teukolsky, S. A. 2010a, Classical and Quantum Gravity, 27, 114106
Duez, V., Braithwaite, J., & Mathis, S. 2010b, ApJ, 724, L34
Ferrario, L., de Martino, D., & Gänsicke, B. T. 2015, Space Sci. Rev., 191, 111
Fesen, R. A., Hoeflich, P. A., Hamilton, A. J. S., et al. 2007, ApJ, 658, 396
Fesen, R. A., Höflich, P. A., & Hamilton, A. J. S. 2015, ApJ, 804, 140
Fisher, A., Branch, D., Nugent, P., & Baron, E. 1997, ApJ, 481, L89
Foley, R. J., Challis, P. J., Chornock, R., et al. 2013, ApJ, 767, 57
Franzon, B., & Schramm, S. 2017, ArXiv e-prints
Gamezo, V. N., Khokhlov, A. M., & Oran, E. S. 2005, ApJ, 623, 337
Gamezo, V. N., Khokhlov, A. M., Oran, E. S., Ctchelkanova, A. Y., & Rosenberg, R. O. 2003, Science, 299, 77
Gardiner, T. A., & Stone, J. M. 2005, J. Comput. Phys, 205, 509
Ghezzi, C. R., de Gouveia Dal Pino, E. M., & Horvath, J. E. 2001, ApJ, 548, L193
—. 2004, MNRAS, 348, 451
Giammichele, N., Bergeron, P., & Dufour, P. 2012, ApJS, 199, 29
Hawley, J. F., Gammie, C. F., & Balbus, S. A. 1996, ApJ, 464, 690
Hicks, E. P. 2015, ApJ, 803, 72
Hoeflich, P. 1995, ApJ, 443, 89
—. 2006, Nuclear Physics A, 777, 579
Hoeflich, P., Gerardy, C. L., Fesen, R. A., & Sakai, S. 2002, ApJ, 568, 791
Hoeflich, P., Gerardy, C. L., Nomoto, K., et al. 2004, ApJ, 617, 1258
Hoeflich, P., & Khokhlov, A. 1996, ApJ, 457, 500
Hoeflich, P., & Stein, J. 2002, ApJ, 568, 779
Hoeflich, P., Hsiao, E. Y., Ashall, C., et al. 2017, ApJ, 846, 58
Höflich, P., Gerardy, C. L., Marion, H., & Quimby, R. 2006, New A Rev., 50, 470
Howell, D. A., Hoeflich, P., Wang, L., & Wheeler, J. C. 2001, ApJ, 556, 302
Howell, D. A., Sullivan, M., Nugent, P. E., et al. 2006, Nature, 443, 308
Hoyle, F., & Fowler, W. A. 1960, ApJ, 132, 565
Hristov, B., Collins, D. C., Hoeflich, P., & Weatherford, C. 2016, in American Astronomical Society Meeting Abstracts, Vol. 227, American Astronomical Society Meeting Abstracts, 237.16
Hunter, J. D. 2007, Computing In Science & Engineering, 9, 90
Iben, Jr., I., & Tutukov, A. V. 1984, ApJS, 54, 335
Isern, J., García-Berro, E., Külebi, B., & Lorén-Aguilar, P. 2017, ArXiv e-prints
Isern, J., Hernanz, M., & José, J. 2011, in Lecture Notes in Physics, Berlin Springer Verlag, Vol. 812, Lecture Notes in Physics, Berlin Springer Verlag, ed. R. Diehl, D. H. Hartmann, & N. Prantzos, 233–308
Ji, S., Fisher, R. T., García-Berro, E., et al. 2013, ApJ, 773, 136
Kawka, A., Vennes, S., Schmidt, G. D., Wickramasinghe, D. T., & Koch, R. 2007, ApJ, 654, 499
Kazantsev, A. P. 1968, Soviet Journal of Experimental and Theoretical Physics, 26, 1031
Kepler, S. O., Pelisoli, I., Jordan, S., et al. 2013, MNRAS, 429, 2934
Kepler, S. O., Pelisoli, I., Koester, D., et al. 2016, MNRAS, 455, 3413
Kerzendorf, W. E., McCully, C., Taubenberger, S., et al. 2017, MNRAS, 472, 2534
Khokhlov, A. M. 1995, ApJ, 449, 695
Khokhlov, A. M., Oran, E. S., & Wheeler, J. C. 1997, ApJ, 478, 678
Kirshner, R. P., Jeffery, D. J., Leibundgut, B., et al. 1993, ApJ, 415, 589
Kritsuk, A. G., Norman, M. L., Padoan, P., & Wagner, R. 2007, ApJ, 665, 416
Kromer, M., Sim, S. A., Fink, M., et al. 2010, ApJ, 719, 1067
Kutsuna, M., & Shigeyama, T. 2012, ApJ, 749, 51
Li, S., Li, H., & Cen, R. 2008, ApJS, 174, 1
Li, W., Filippenko, A. V., Chornock, R., & Jha, S. 2003, PASP, 115, 844
Li, W., Bloom, J. S., Podsiadlowski, P., et al. 2011, Nature, 480, 348
Liebert, J., Bergeron, P., & Holberg, J. B. 2003, AJ, 125, 348
Livne, E. 1990, ApJ, 354, L53
—. 1999, ApJ, 527, L97
Lorén-Aguilar, P., Isern, J., & García-Berro, E. 2009, A&A, 500, 1193
Maeda, K., Benetti, S., Stritzinger, M., et al. 2010, Nature, 466, 82
Maeda, K., Leloudas, G., Taubenberger, S., et al. 2011, MNRAS, 413, 3075
Marion, G. H., Hoeflich, P., Vacca, W. D., & Wheeler, J. C. 2003, ApJ, 591, 316
Maund, J. R., Hoeflich, P. A., Patat, F., et al. 2010, ApJ, 725, L167
Mignone, A. 2007, J. Comput. Phys, 225, 1427
Milne, P., The, L.-S., & Leising, M. 1999, ApJS, 124, 503
Motohara, K., Maeda, K., Gerardy, C. L., et al. 2006, ApJ, 652, L101
Nandkumar, R., & Pethick, C. J. 1984, MNRAS, 209, 511
Niemeyer, J. C., & Hillebrandt, W. 1995, ApJ, 452, 769
Niemeyer, J. C., & Woosley, S. E. 1997, ApJ, 475, 740
Nomoto, K. 1982a, ApJ, 257, 780
—. 1982b, ApJ, 253, 798
Norman, M. L., Reynolds, D. R., So, G. C., Harkness, R. P., & Wise, J. H. 2015, ApJS, 216, 16

O'Shea, B. W., Wise, J. H., Xu, H., & Norman, M. L. 2015, ApJ, 807, L12
Pakmor, R., Hachinger, S., Röpke, F. K., & Hillebrandt, W. 2011, A&A, 528, A117
Parker, E. N. 1979, Cosmical magnetic fields: Their origin and their activity (New York: Oxford University Press)
Patat, F., Hoeflich, P., Baade, D., et al. 2012, A&A, 545, A7
Penney, R., & Hoeflich, P. 2014, ApJ, 795, 84
Phillips, M. M. 1993, ApJ, 413, L105
Piersanti, L., Gagliardi, S., Iben, Jr., I., & Tornambé, A. 2003, ApJ, 598, 1229
Plewa, T. 2007, ApJ, 657, 942
Poludnenko, A. 2016, Handbook of Supernovae, ed. P. Murdin (Springer, Berlin), 999
Poludnenko, A. Y., & Oran, E. S. 2011, ArXiv e-prints
Potekhin, A. Y., & Chabrier, G. 2012, A&A, 538, A115
Rasio, F. A., & Shapiro, S. L. 1994, ApJ, 432, 242
Reinecke, M., Hillebrandt, W., & Niemeyer, J. C. 1999, A&A, 347, 739
Reinsch, K., Euchner, F., Beuermann, K., Jordan, S., & Gänsicke, B. T. 2005, in Astronomical Society of the Pacific Conference Series, Vol. 330, The Astrophysics of Cataclysmic Variables and Related Objects, ed. J.-M. Hameury & J.-P. Lasota, 177
Remming, I. S., & Khokhlov, A. M. 2014, ApJ, 794, 87
—. 2016, ApJ, 831, 162
Rest, A., Suntzeff, N. B., Olsen, K., et al. 2005, Nature, 438, 1132
Rest, A., Matheson, T., Blondin, S., et al. 2008, ApJ, 680, 1137
Röpke, F. K., Gieseler, M., Reinecke, M., Travaglio, C., & Hillebrandt, W. 2006, A&A, 453, 203
Röpke, F. K., Kromer, M., Seitenzahl, I. R., et al. 2012, ApJ, 750, L19
Schekochihin, A. A., & Cowley, S. C. 2007, Turbulence and Magnetic Fields in Astrophysical Plasmas, ed. S. Molokov, R. Moreau, & H. K. Moffatt (Springer), 85
Schober, J., Schleicher, D., Bovino, S., & Klessen, R. S. 2012, Phys. Rev. E, 86, 066412
Schober, J., Schleicher, D. R. G., Federrath, C., Bovino, S., & Klessen, R. S. 2015, Phys. Rev. E, 92, 023010
Segretain, L., Chabrier, G., & Mochkovitch, R. 1997, ApJ, 481, 355
Sion, E. M., Holberg, J. B., Oswalt, T. D., et al. 2014, AJ, 147, 129
Spruit, H. C. 2002, A&A, 381, 923
Stehle, M., Mazzali, P. A., Benetti, S., & Hillebrandt, W. 2005, MNRAS, 360, 1231
Stone, J. M., & Gardiner, T. 2007a, Physics of Fluid Dynamics Letters, 19, 094104
—. 2007b, ApJ, 671, 1726
—. 2007c, ApJ, 671, 1726
Stritzinger, M. D., Hsiao, E., Valenti, S., et al. 2014, A&A, 561, A146
Subramanian, K. 1999, Physical Review Letters, 83, 2957
Sugimoto, D., & Nomoto, K. 1980, Space Sci. Rev., 25, 155
Tanaka, M., Mazzali, P. A., Stanishev, V., et al. 2011, MNRAS, 410, 1725
Tayler, R. J. 1973, MNRAS, 161, 365
Thomas, J. H., Markiel, J. A., & van Horn, H. M. 1995, ApJ, 453, 403
Timmes, & Woosley. 1992, ApJ, 396, 649
Turk, M. J., Smith, B. D., Oishi, J. S., et al. 2011, ApJS, 192, 9
Van Der Walt, S., Colbert, S. C., & Varoquaux, G. 2011, ArXiv e-prints
Wang, B., Chen, X., Meng, X., & Han, Z. 2009a, ApJ, 701, 1540
Wang, B., Meng, X., Chen, X., & Han, Z. 2009b, MNRAS, 395, 847
Webbink, R. F. 1984, ApJ, 277, 355
Whelan, J., & Iben, I. J. 1973, ApJ, 186, 1007
Woosley, S. E., & Kasen, D. 2011, ApJ, 734, 38
Woosley, S. E., & Weaver, T. A. 1994, ApJ, 423, 371
Woosley, S. E., Weaver, T. A., & Taam, R. E. 1980, in Texas Workshop on Type I Supernovae, ed. J. C. Wheeler, 96–112
Yang, Y., Wang, L., Baade, D., et al. 2017, ArXiv e-prints
Yoon, S.-C., Podsiadlowski, P., & Rosswog, S. 2007, MNRAS, 380, 933
Zhu, C., Pakmor, R., van Kerkwijk, M. H., & Chang, P. 2015, ApJ, 806, L1